Nanoscale

51
Sb
121.76

ROYAL SOCIETY
OF CHEMISTRY

PAPER
Inmaculada Andreu, Gonzalo Abellán *et al.*
Interplay between the oxidation process and cytotoxic
effects of antimonene nanomaterials

NCNST

Check for updates

Interplay between the oxidation process and cytotoxic effects of antimonene nanomaterials†

Pau Congost-Escoin, [a] Matteo Andrea Lucherelli, [a] Víctor Oestreicher, [a] Guillermo García-Lainez, [b] Marta Alcaraz, [a] Martín Mizrahi, [c,d] Maria Varela, [e] Inmaculada Andreu *[f,g] and Gonzalo Abellán *[a]

Pnictogen nanomaterials have recently attracted researchers' attention owing to their promising properties in the field of electronic, energy storage, and nanomedicine applications. Moreover, especially in the case of heavy pnictogens, their chemistry allows for nanomaterial synthesis using both top-down and bottom-up approaches, yielding materials with remarkable differences in terms of morphology, size, yield, and properties. In this study, we carried out a comprehensive structural and spectroscopic characterization of antimony-based nanomaterials (Sb-nanomaterials) obtained by applying different production methodologies (bottom-up and top-down routes) and investigating the influence of the synthesis on their oxidation state and stability in a biological environment. Indeed, *in situ* XANES/EXAFS studies of Sb-nanomaterials incubated in cell culture media were carried out, unveiling a different oxidation behavior. Furthermore, we investigated the cytotoxic effects of Sb-nanomaterials on six different cell lines: two non-cancerous (FSK and HEK293) and four cancerous (HeLa, SKBR3, THP-1, and A549). The results reveal that hexagonal antimonene (Sb-H) synthesized using a colloidal approach oxidizes the most and faster in cell culture media compared to liquid phase exfoliated (LPE) antimonene, suffering acute degradation and anticipating well-differentiated toxicity from its peers. In addition, the study highlights the importance of the synthetic route for the Sb-nanomaterials as it was observed to influence the chemical evolution of Sb-H into toxic Sb oxide species, playing a critical role in its ability to rapidly eliminate tumor cells. These findings provide insights into the mechanisms underlying the dark cytotoxicity of Sb-H and other related Sb-nanomaterials, underlining the importance of developing therapies based on controlled and on-demand nanomaterial oxidation.

Introduction

Since the first isolation of graphene in 2004,[1] two-dimensional (2D) materials have received increasing attention owing to

[a] *Instituto de Ciencia Molecular (ICMol), Universitat de València, Catedrático José Beltrán Martínez no. 2, 46980 Paterna, Spain. E-mail: gonzalo.abellan@uv.es*
[b] *Instituto de Investigación Sanitaria (IIS) La Fe, Hospital Universitari i Politècnic La Fe, Avenida de Fernando Abril Martorell 106, 46026 Valencia, Spain*
[c] *Instituto de Investigaciones Fisicoquímicas Técnicas y Aplicadas (INIFTA), Departamento de Química, Facultad de Ciencias Exactas. Universidad Nacional de La Plata, CCT La Plata- CONICET. Diagonal 113 y 64, 1900 La Plata, Argentina*
[d] *Facultad de Ingeniería, Universidad Nacional de La Plata, Calle 1 esq. 47, 1900 La Plata, Argentina*
[e] *Instituto Pluridisciplinar & Departamento de Física de Materiales, Universidad Complutense de Madrid (UCM), 28040 Madrid, Spain*
[f] *Departamento de Química-Universitat Politècnica de València, Camino de Vera s/n, 46022, Valencia, Spain. E-mail: iandreur@qim.upv.es*
[g] *Unidad Mixta de Investigación. Universitat Politècnica de València -Instituto de Investigación Sanitaria La Fe, Hospital Universitari i Politècnic La Fe, Avenida de Fernando Abril Martorell 106, 46026 Valencia, Spain*
† Electronic supplementary information (ESI) available. See DOI: https://doi.org/10.1039/d4nr00532e

their unique physical and chemical properties.[2,3] Numerous members have been added to the family of 2D materials in recent years, spanning from graphene and its derivatives to post-graphene materials such as transition metal dichalcogenides (TMDCs), MXenes, layered (hydro)oxides, metal-organic frameworks and, more recently, pnictogens (Pn).[4] Among these, 2D pnictogens (P, As, Sb and Bi) present an interesting combination of structural flexibility and tunable properties, with a layer-dependent bandgap, spin–orbit coupling, and high theoretical capacity for electron charging. In addition, their chemical reactivity, organic molecule stabilization and light-conversion properties can be exploited in the field of nanomedicine for drug delivery platforms, biosensors and theranostic agents.[3–5] Nanomedicine combines the properties of molecular drugs with the unique properties of nanomaterials, providing synergistic effects for enhanced therapeutic efficiency.[6] Pnictogen chemistry can play an important role in biomedical applications by taking advantage of the different interactions of each element with the biological environment.[4] Moreover, physicochemical properties, such as chemical composition, size, shape, charge or surface chem-

istry, are key factors determining the nanomaterial biomedical performance, influencing both *in vivo* and *in vitro* uptake, fate and toxicity.[7] Phosphorene, the first and most studied member of the 2D-Pn family, has demonstrated great potential in nanomedicine owing to its intrinsic fluorescence and non-toxic *in vivo* biodegradation.[8–10] In this line, few-layer antimonene is postulated as a counterpart to phosphorene in the field of nanomedicine. Indeed, its optical and electronic properties match or even surpass phosphorene's.[11] Its peerless allotropy[12,13] and rich chemical reactivity[14,15] make it an ideal candidate for multimodal cancer therapies based on photodynamic therapy (PDT). In addition, the broad and strong absorption from the ultraviolet (UV) to the near-infrared (NIR) wavelengths results in the highest photothermal conversion efficiency (PTCE, ~45.5%) among Xenes and other 2D materials, making few-layer antimonene a promising agent for photothermal therapy (PTT)[16] and as a photoacoustic imaging (PAI) agent.[17] However, these applications are mainly based on their physical properties (PTT and PAI), or photo-induced activation (PDT), rather than the direct toxicity of the material (*i.e.* chemotherapy). In addition, Sb oxide species (Sb_2O_3 and Sb_2O_5) are known to pose potential risks to human health, exerting toxic effects in human tissues,[11,18–22] and can be generated by *in situ* controlled laser irradiation.[23,24] It is, therefore, important to remark that the PTT and PDT efficiency of Sb-nanomaterials could benefit from the toxic effects exerted by the produced Sb oxides owing to their chemotherapeutic synergistic effect (dark cytotoxicity).

Nevertheless, the dark cytotoxicity of Sb-nanomaterials suffers from a lack of data and disparity of information, with most studies focusing on coated or functionalized materials, aimed at improving biocompatibility but neglecting the effect of the non-coated nanomaterial in cells. To the best of our knowledge, the only report in as-synthesized Sb nanosheet cytotoxicity demonstrated a viability of ~60% for A549 lung cancer cells.[25] In contrast, functionalized or coated Sb nano-materials showed no clear signs of cytotoxicity regardless of the coating used.[16,19,21,22,26]

The present work aims to perform for the first time an exhaustive investigation of Sb-based nanomaterial cytotoxicity. Herein, we paid special attention to the synthesis and advanced characterization of different Sb-nanomaterials, assessing an extended cytotoxicity evaluation based on their physicochemical properties, such as size, morphology and oxidation behavior. The nanomaterial object of our study was prepared by employing the most significant synthetic routes reported to date, yielding few-layer Sb with hexagonal morphology (Sb-H, obtained by bottom-up colloidal synthesis)[27] Sb-nanosheets (Sb-NS, prepared by liquid phase exfoliation, LPE)[27] and nanoparticles (Sb-NP, prepared by LPE and cascade centrifugation)[16,28] (Scheme 1). Their cytotoxicity was assessed in six cell lines, including both tumor (HeLa, SKBR3, THP-1, and A549) and non-tumor (FSK and HEK293), revealing a broad cytotoxic effect of Sb-nanomaterials on tumor cell lines. The Sb-nanomaterial oxidation behavior was investigated under biological conditions using *in situ* synchrotron X-ray absorption spectroscopy (XAS), discovering different oxidative behaviors and correlating them with their dark cytotoxicity. Finally, we studied the mechanisms involved in their cytotoxic effects through enzymatic activity studies and cellular reactive oxygen species (ROS) production after treatment. The scientific multidisciplinary approach reported in this study provides novel characterization methodologies and contributes to deciphering the chemotherapeutic potential role of Sb-nanomaterials, paving the way for their biomedical applications.

Results and discussion

Sb nanomaterial synthesis and characterization

Few-layer Sb Hexagons (Sb-H) were synthesized by applying a bottom-up method optimized by our group.[27] This approach
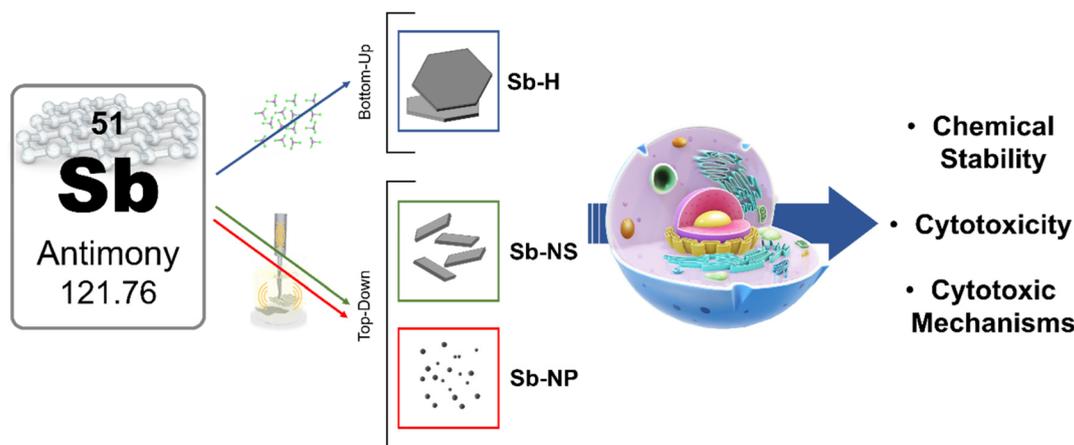
Scheme 1 Schematic representation of the experiments conducted in this study. Three different Sb nanomaterials were synthesized using different methodologies and their stability, cytotoxicity, and cytotoxic mechanisms were investigated in different cell lines.

permits starting from Sb-salt (SbCl$_3$) and organic molecules to synthesize reproducible, thin, regular and uniform hexagonal particles composed mainly of metallic Sb covered with an organic passivation layer of thiol-bonded dodecanethiols.[27,29,30] For the biological comparison, Sb-NS and Sb-NP were produced following previously reported literature, among which we selected studies that included cytotoxicity assays.[13,21,26] Both materials were obtained by the application of sonication cycles in organic solvents at different times (see Methods section for the synthetic details).

The characterization of the nanomaterials was conducted by several microscopic and spectroscopic techniques, including transmission electron microscopy (TEM), dynamic light scattering (DLS), electron energy-loss spectroscopy (EELS), X-ray diffraction (XRD), Raman spectroscopy, X-ray photoelectron spectroscopy (XPS) and X-ray absorption spectroscopy (XAS).

In this context, TEM images of the Sb-nanomaterials confirmed that Sb-H presents regular hexagonal morphology (Fig. 1A). The particle sizes obtained from TEM images (Fig. 1D) show a homogeneous size distribution in the range of 800–1000 nm. However, Sb-NS exhibits non-homogeneous morphology with the distribution of unregular edges and sizes ranging from few nm up to 400 nm, with an average population of ~100 nm (Fig. 1B and E), which agrees with previous reports.[13] Regarding Sb-NP, the particles are characterized by non-homogeneous roundish and elongated morphology, with lateral sizes between 7 and 17 nm (Fig. 1C and F). DLS was employed to compare the ensemble solution to statistical TEM images (Fig. 1G–I). In the case of Sb-H, two different populations are present. The largest (~1 μm) corresponds to the hexagonal particles, while the smaller (~200 nm) corresponds to particles of tetragonal morphologies, a secondary product
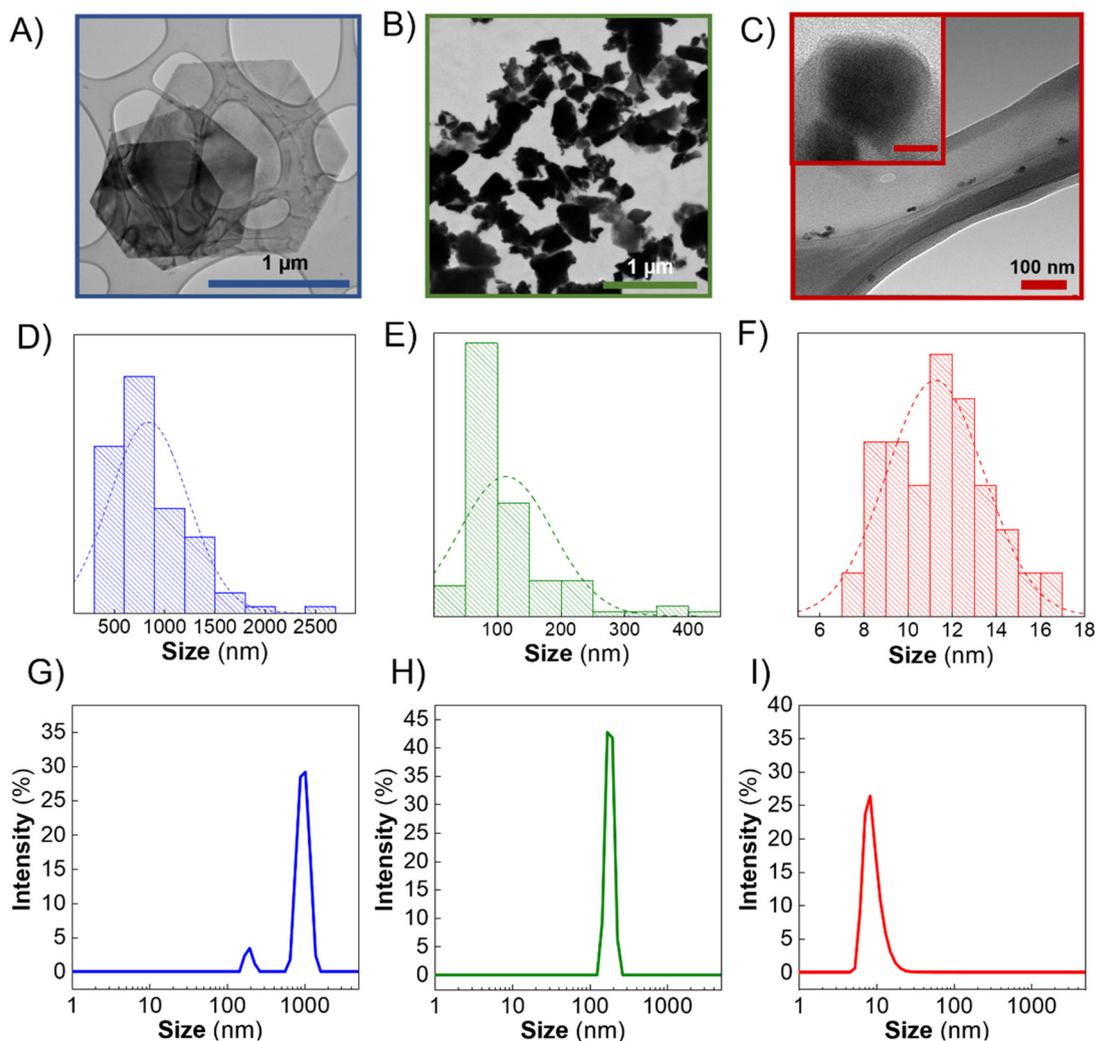

Fig. 1 TEM images of Sb nanomaterials and size distribution obtained from statistics TEM and DLS. (A), (B), and (C) TEM images of Sb-H, Sb-NS, and Sb-NP. Scale bar dimension is adapted for the best nanoparticle resolution. Inset in (C) shows an HRTEM image of the Sb-NP (scale bar of the inset 10 nm). (D), (E), and (F) Lateral size distribution of the Sb-nanomaterials obtained from the TEM images: Sb-H, Sb-NS, and Sb-NP (from left to right). Scalebars are different to better adapt to each distribution; (G), (H) and (I) DLS hydrodynamic radius of Sb-H, Sb-NS, and Sb-NP.

formed from the colloidal synthesis, corresponding to ~40% of the particles.[27] For the LPE nanomaterials, Sb-NP presents an average population of ~10 nm and Sb-NS of ~150 nm. As expected, Sb-H presents a regular shape and good lateral size distribution similar to Sb-NP, resulting in the most homogeneous materials in terms of lateral size. Finally, Sb-NS resulted in the most heterogeneous material in terms of size and shape. Remarkably, the hydrodynamic size obtained by DLS (polydispersity indexes: Sb-H = 0.366, Sb-NS = 1 and Sb-NP = 0.341) is in accordance with the TEM lateral size distribution, suggesting that this technique could be employed for the statistic particle size characterization of Sb-nanomaterials without any further data treatment, as previously reported for other 2D materials.[31] Regarding the thickness of the nanomaterials, Sb-NP showed an average thickness of ~10 nm, followed by Sb-NS with an average thickness of ~19 nm,[28] and Sb-H with an average value of around 20 nm (Fig. S2†).[27]

To further investigate the morphology and structure of the different Sb nanomaterials, scanning transmission electron microscopy (STEM) was employed. A microscope equipped with a high-angle annular dark field (HAADF) detector was operated at an acceleration voltage of 80 kV, preventing electron beam-induced damage to the nanomaterials (Fig. 2). High-magnification HAADF images show a high degree of crystallinity, with no major defects within the three nanomaterials (Fig. 2B, G, and L). Partial defects were exhibited at the edges of Sb-NS and Sb-NP with the presence of a nanometric amorphous region (Fig. 2H and M), which was previously observed also for the Sb-H.[27] The chemical composition of the Sb-H, Sb-NS and Sb-NP was determined by electron energy-loss spectroscopy (EELS), obtaining the Sb $M_{4,5}$, and O K elemental maps (Fig. 2). Sb-H is mainly composed of Sb and a small amount of oxygen homogeneously distributed on the surface and edges of the nanosheet, indicating the presence of a native oxidation layer of Sb_2O_3, as previously reported, which is obtained from the quantitative analysis of the EELS maps.[24,32] In fact, detailed analyses of the atomic composition (atomic percentage) revealed a homogeneous distribution of the oxide layer on the particle surface (Fig. 2E), with histograms centered at an average of 50%–50% Sb–O ratio, with a fairly wide distribution of values. In the case of the Sb-NS, EELS maps confirm that the amorphous layer located at the edge of the sheets is composed of Sb and O, appearing larger than the Sb-H samples (annular bright field (ABF) images, Fig. 2H). This very same situation is observed in the case of Sb-NP, presenting smaller amorphous edges. Overall, Sb-H shows a more homogeneous surface oxidation compared to the Sb-NS and Sb-NP, with a higher amount of amorphous oxides on the edges.

The XRD patterns of the pristine Sb-nanomaterials revealed their prominent metallic nature, showing the crystalline structure of β-antimony (Fig. 3A). The analysis of the FHMW of the main peak (110) revealed different sizes of the crystallite, with values of 51.45 nm, 46.31 nm and 37.58 nm for the Sb-H, Sb-NP and Sb-NS, respectively. Besides, XRD can only analyze crystalline structures, veiling other amorphous matter as oxide
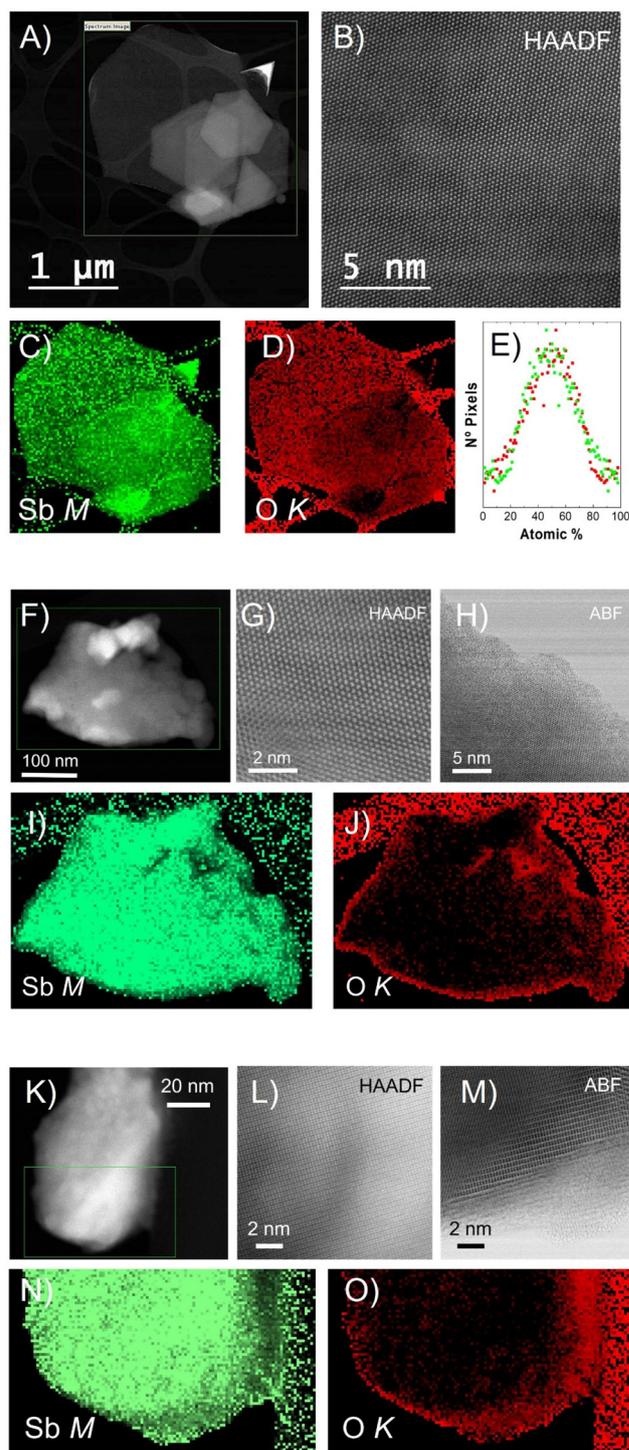

Fig. 2 STEM image of Sb-H, Sb-NS and Sb-NP. (A) HAADF image of Sb-H. (B) High resolution image of the Sb-H sample with a high degree of crystallinity. (C) EELS mappings of the Sb $M_{4,5}$ edge (D) and O K edge. (E) Histograms of the Sb (green) and O (red) images shown in C and D, respectively. (F) STEM images of Sb-NS. (G) HAADF image of the crystalline structure of Sb-NS. (H) ABF high resolution image acquired on the top edge of the particles. (I) EELS mappings of the Sb M edge and (J) O K edge. (K) STEM images of the Sb-NP. (L) HAADF image of the crystalline structure of Sb-NS. (M) ABF high resolution image acquired on the bottom edge of the particles. (N) EELS mappings of the Sb M edge and (O) O K edge.
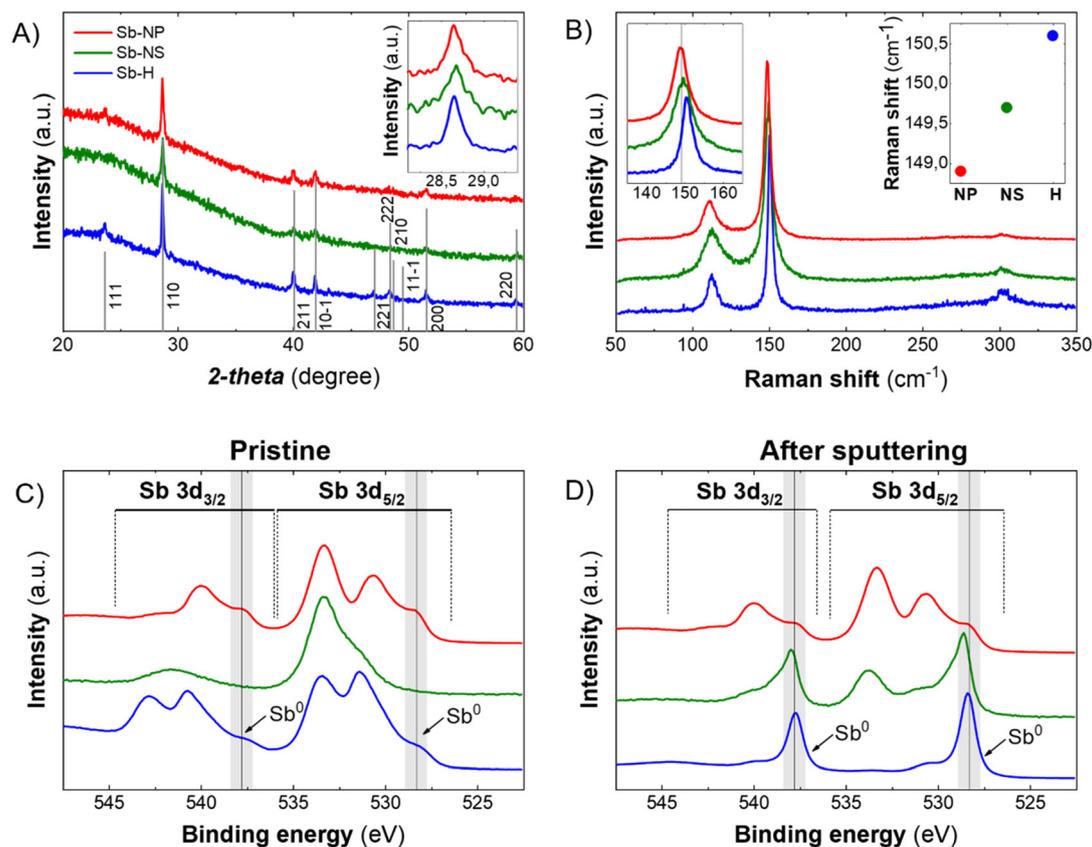
Fig. 3 (A) XRD diffractogram of the Sb-nanomaterials. Inset shows a detail of the 110 diffraction peaks. (B) Raman spectra of the nanomaterials. Insets show the details of the A_{1g} peak (left) and the Raman shift value of the A_{1g} peak (right). (C) XPS spectra of Sb nanomaterials as-synthesized and (D) after an Ar sputtering process in UHV.

traces. However, the oxidation state of the particles strongly depends on the production methodology and could play a fundamental role in its biomedical behaviour, making important the detection of these species. Raman spectroscopy can partially address this issue because metallic and oxide Sb are characterized by different vibrational modes. Sb(0) presents two well-defined vibrational modes, E_g (in-plane vibrations, $\sim$110 cm^{-1}) and A_{1g} (out of plane vibrations, $\sim$145–150 cm^{-1}), while Sb_2O_3 and Sb_2O_5 exhibit different signals in the range of 190–450 cm^{-1}.[32] All the three materials present the two main phonon peaks of antimonene at $\sim$112.2 cm^{-1} and $\sim$150.1 cm^{-1} (Fig. 3B), while oxidized species could not be detected (Fig. S3†) despite their presence observed by EELS analysis and are reported to be spontaneous when Sb nanomaterials are exposed to air.[13,24,32,33] Thus, to improve the characterization of the materials and reveal the antimony oxide species, XPS was carried out as surface analysis (Fig. S4 and 5†). The analysis was performed on the materials as produced (Fig. 3C) and after the Ar sputtering process (Fig. 3D), partially removing the outer surface layers and permitting an in-depth analysis. The three nanomaterials show the presence of Sb oxide species on the surface, with different degrees of oxidation depending on the synthetic method (Fig. S4†). In the case of Sb-H, we can observe a peak at 531.6 eV that is not present in

the case of the Sb-NP and Sb-NS. Its slight shift to higher energies with respect to the Sb_2O_3 peak suggests the detection of the Sb–S bond, which is slightly higher in energy compared to the Sb–O,[34] related to the thiol-bonded organic passivation layer present as a result of Sb-H chemical synthesis.[27,30] As expected, the presence of metallic Sb increases and becomes predominant after the sputtering process, being Sb-H the specie with the higher Sb^0 content (80.16%), while Sb-NS presented 13.63 of metallic Sb after the sputtering but still a relevant oxygen content (13.61%) (Table 1). This suggests that oxidation is mostly relegated to the surface and edges of the materials, acting also as a protective layer that hinders the complete oxidation of the particles, which maintains the core of Sb(0). Notably, Sb-NP showed the presence of both metallic (16.88%) and oxidized Sb (80.68%) even after the sputtering process. This behavior is probably due to their small dimension, which leads to exposing a great amount of surface compared to the particle core after sputtering, resulting in a major oxide content. The role of this oxidized surface is further discussed in the cytotoxic mechanisms section.

The discrepancy between Raman and XPS results could be attributed to a small amount of surface oxides compared to the total amount of metallic antimony in the whole particle. However, these two techniques are the most commonly

Table 1 Atomic % composition of the Sb-nanomaterial surface. Data are reported in pristine form and after 10 cycles of sputtering with an Ar beam. Percentages are evaluated on Sb3d/Sb4d, O1s and C1s peaks

Sb-H		Sb-NS		Sb-NP	
Pristine	Sputtering	Pristine	Sputtering	Pristine	Sputtering
47.32	80.13	2.12	13.63	7.93	16.89
25.37	8.06	21.77	13.61	66.98	80.69
27.31	11.81	76.11	72.76	25.08	2.42

employed for the characterization of pnictogens, and it is now clear that their combination is not sufficient for an accurate evaluation of their oxidation state, especially in the case of potential bias due to the morphology of the particles. In this regard, X-ray Absorption Spectroscopy (XAS) permits analysis of the material's ensemble, providing insights into the oxidation state and short-range crystallographic structure. Herein, we report the XANES (X-ray Absorption Near Edge Structure) measured at the BL-22 (CLÆSS) beamline from the ALBA synchrotron (Barcelona – Spain). The as-synthesized Sb-H, Sb-NS and Sb-NP XANES spectra, taken at the Sb K-edge, are shown in Fig. 4A. All three materials exhibit a small shift in the absorption edge position toward higher energy with respect to Sb^0, which can be interpreted as an increase in the average oxidation state in the samples. Using the integral method, it is possible to estimate the average oxidation state of the material,[35] which was in the order of +0.4 for all the samples studied. Furthermore, EXAFS (Extended X-ray Absorption Fine Structure) analysis allows us to study the structure of the sample by analyzing the interaction between the ejected photoelectron and the surrounding non-excited atoms. This interaction generates an oscillation in the region behind the absorption edge, which is related to the type, amount and distance of the atoms neighboring the absorbing atom. The Fourier transform (FT) of this oscillation provides information about the crystallographic structure around the absorbing atom (Fig. 4B). A simple inspection of the FTs shows the presence of a main peak in the Sb-H and Sb-NP samples at approximately 2.75 Å (without phase correction), which coincides with the characteristic distance of Sb^0. Furthermore, in both samples, the presence of a lower magnitude contribution can be observed in the region in which the Sb oxide reference samples present their main peak, which is associated with the Sb–O distance. Interestingly, the Sb–O distance seems to be different for the Sb-H and Sb-NP (1.5 Å and 1.3 Å, respectively), indicating a slightly different structure of the oxidated layer on the surface of the nanomaterials.

In summary, XANES and EXAFS analysis provides a realistic description of the chemical composition of the materials, complementing the observations obtained by the combination of Raman, XRD and XPS techniques. Antimony-based nanomaterials mainly constitute metallic Sb, coated by Sb oxide species in a very similar proportion, independent of the synthetic method used. The last ones are almost invisible for Raman and XRD but represent the most prominent com-
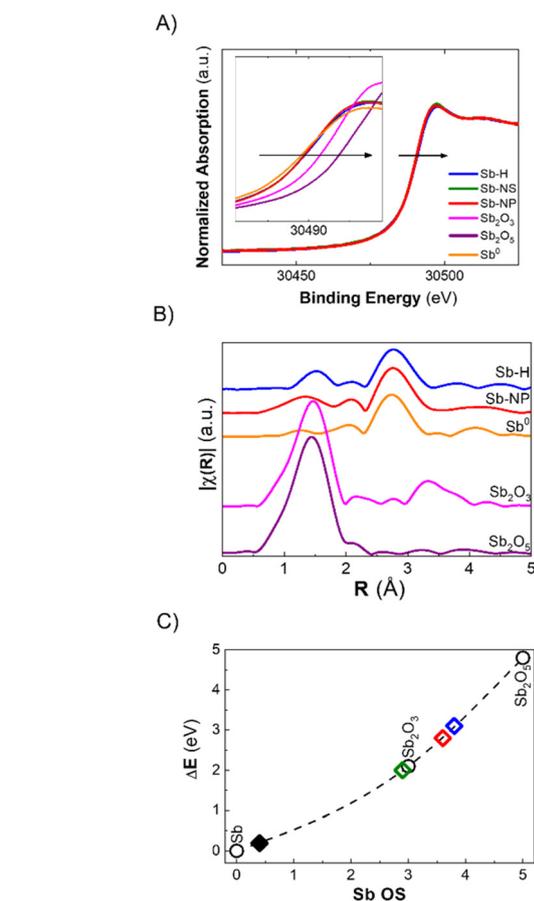

Fig. 4 (A) XANES of the Sb-H, Sb-NS and Sb-NP. Inset shows the XANES region of the spectrum of the Sb-nanomaterials compared to Sb references (Sb^0, Sb_2O_3 and Sb_2O_5). The arrow indicates the energy shift to higher energies upon oxidation. (B) Fourier transform of the extracted κ^2-weighted EXAFS oscillation fittings in the Sb K-edge. (C) Comparison of the final oxidation state (OS) of Sb-nanomaterials obtained by *ex situ* XANES: open circles indicate Sb reference compounds, black filled diamond indicates the initial OS of the Sb-nanomaterials, and open diamonds show their final OS.

ponent of the surfaces, as revealed by XPS, according to the characteristics of each technique.

Stability and chemical evolution in cell culture media

As previously mentioned, the Sb oxide passivation layer plays a fundamental role in Sb-nanomaterial environmental stability,

shielding Sb^0 from oxygen (oppositely to the case of black phosphorus),[36] with significant consequences in biological systems.[14,24,37] However, the stability of few-layer antimonene remains a matter of debate in the scientific community.[11] Although some researchers claim the great stability of few-layer antimonene under ambient conditions and water,[12] other studies have reported the oxidation of Sb-nanomaterials in cellular environments (*i.e.* under normoxic conditions).[22] The amount of oxide species is influenced by the production methodology; nevertheless, their behaviour under physiological conditions is unknown, representing a key point for Sb-nanomaterial biomedical applications. During the incubation with cells, and without a proper coating, few-layer antimonene interacts directly with the complex and oxidative environment constituting the cell culture media (an aqueous media containing many molecules, such as sugars, peptides, proteins and salts), causing its chemical evolution. Consequently, we investigated the behaviour of as-synthesized Sb-nanomaterials under biological conditions by applying *in situ* XANES. The experiment was also performed at CLÆSS (BL-22) in ALBA synchrotron facilities, which allows real-time monitoring of the mean oxidation state during the incubation process, indicating the stability of this material under the biological milieu.

To properly compare the *in situ* measurements, *ex situ* references were first analyzed to obtain clear information about the initial and final oxidation states of the compounds under analysis. The oxidation state of the fresh synthesized Sb-nanomaterials, as well as of diverse compounds of antimony at oxidation state 0, III and V (Sb^0, Sb_2O_3, Sb_2O_5, and $Sb(CH_3COO^-)_3$), and of their final state after 1 week of incubation (37 °C) in cell culture media was measured. These provided accurate references of antimony for a comparison with the *in situ* oxidation experiments (Fig. 4C and S6†). Interestingly, after one week of incubation, each nanomaterial exhibited a different degree of oxidation. Sb-H and Sb-NP showed similar behavior, being the most oxidized ones (average OS of +3.8 and +3.6, respectively), indicating the formation of both Sb species, trivalent and pentavalent. In contrast, Sb-NS exhibited a lower oxidation state (OS +2.9), suggesting the formation of only trivalent Sb.

To gain a better understanding of the oxidation process, *in situ* XANES kinetic measurements were carried out in cell culture media for the Sb-H and Sb-NP samples (Fig. 5A and B). Unfortunately, this was not possible for Sb-NS due to the low signal obtained. The analysis of these spectra permitted the calculation of the evolution of the oxidation state under biological conditions, revealing different rates of this chemical process for each nanomaterial (Fig. 5C). Thus, Sb-H showed higher and faster oxidation behavior than Sb-NP. Remarkably, Sb-H reached its maximum oxidation state in only 6 hours of incubation (OS after 6 hours: +3.8), while Sb-NP, after the same incubation time, did not reach its final state (OS after 6 hours: +3.2). Furthermore, this process is concomitant with the degradation of hexagonal flakes, as revealed by TEM analysis at different times during incubation (15 minutes, 6, and 24 hours; Fig. S7†). However, LPE-produced Sb-nanomaterials
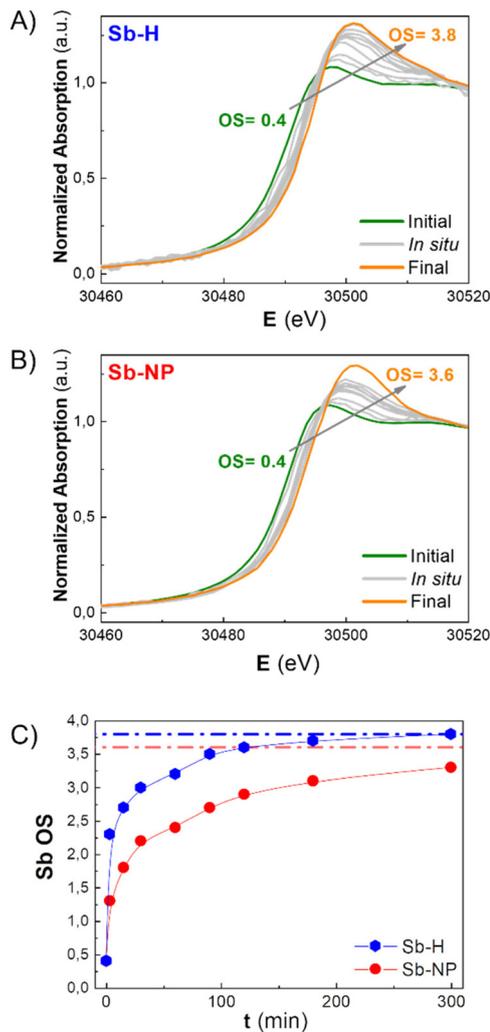

Fig. 5 *In situ* XANES spectra of (A) Sb-H and (B) Sb-NP in cell culture media (37 °C). (C) Time evolution of the oxidation state of Sb-H and Sb-NP obtained from the XANES analysis of the *in situ* measurements. The dotted lines represent the final oxidation state of the Sb-nanomaterials obtained by *ex situ* XANES. A continuous line does not represent a fitting of the data.

did not show significant signs of degradation under the same conditions. These results highlight the improved biodegradability of Sb-H over the LPE Sb-nanomaterials in biological conditions.[38]

These data suggest that the difference in the oxidation process of the Sb-nanomaterials may depend on the chemical nature of their surface layer. Indeed, the Sb-H surface differs from liquid-phase exfoliated Sb-nanomaterials because of its thiol-bonded organic passivation layer.[27,29] This, as shown by the *in situ* XANES, results in faster oxidation and lower stability of the Sb-H compared to the Sb-NP and Sb-NS, which exhibit higher stability under biological conditions, maintaining their morphology even after oxidation. In this regard, the divergence in the final OS observed between Sb-NS and Sb-NP is probably due to the difference in their surface/weight ratio, with Sb-NP having a higher external surface.

Cytotoxic effects of Sb-nanomaterials

Cytotoxicity investigations are primary studies that evaluate the potential effects of nanomaterials in biological environments. As already demonstrated for graphene and other nanomaterials, the morphology, lateral size dimension, thickness, and oxidation degree directly influence the internalization and toxicity of nanomaterials.[39–42] In this framework, bottom-up synthetic procedures are crucial for obtaining reproducible materials and reliable biological performances. To the best of our knowledge, reports on Sb-nanomaterial cytotoxicity are very scarce, with most studies focusing on covalent and non-covalent modified materials,[19,22] leaving a lack of information about the effects of the as-synthesized Sb-nanomaterial.[25] Furthermore, the effects of their physicochemical properties (related to size, shape, and oxidation) on biomedical performance have not yet been investigated. Herein, we performed the first *in vitro* evaluation of the biological effects of Sb-H by investigating its cytotoxicity in six cell lines selected between the most studied cancerous and non-cancerous cell lines. In addition, to compare the effects of materials of different sizes and morphology, we performed the same assays using Sb-NS and NP, permitting an extended comparison of our results with those most recently reported.[16,21,22,22,23,26]

The cell lines employed in this study span among non-cancerous cells (FSK and HEK293) and cancerous cells (HeLa, SKBR3, THP-1, and A549). FSK and HEK293 are derived from human foreskin fibroblasts and suprarenal embryonic cells, respectively. HeLa and A549 are epithelial cells, whose origins are cervical cancer and human alveolar adenocarcinoma, respectively, and both are employed as typical standards for nanomaterial cytotoxicity assays and also for antimony cytotoxicity investigation.[25,43,44] SKBR3 cells are derived from

human breast cancer and are usually used in therapeutic research, while THP-1 cells are monocytes derived from acute leukemia. This wide variety of cell lines in terms of cellular type, size, morphology, and origin is essential to obtain a clear understanding of the effects of the as-synthesized Sb materials in different tumor microenvironments.

The investigation of the cytotoxic effects was conducted for the three nanomaterials at concentrations between 1 and 200 μg mL^{-1} and tested after 24 hours of incubation using the colorimetric MTT cell viability assay (Fig. 6 and S7†), following a similar procedure previously employed for other nanomaterials.[45] For this purpose, SbCl$_3$ was used as a positive control for Sb cellular toxicity, as previously reported for similar studies,[20,25] and also employed as an Sb-H synthetic precursor. Dose–response curves were obtained from the cellular viability assay (Fig. S8†), which was further employed to calculate the half-maximal inhibitory concentrations (IC$_{50}$). The IC$_{50}$ values are shown in Table 2, and they report the concentration of nanomaterial required to reduce the viability of the cell culture by 50% and are employed as a parameter to

Table 2 Compilation of IC$_{50}$ values obtained from the dose–response curves (Fig. S8†) using the GraphPad Prism 8. Values are expressed in μg mL^{-1}. R = cell line resistant to the compound for the tested concentrations

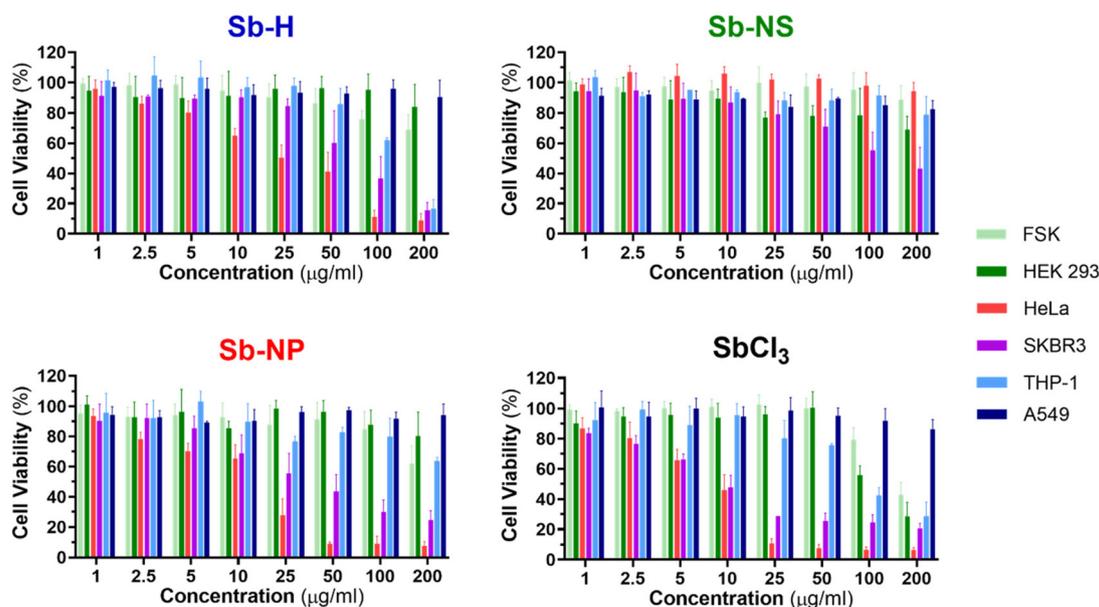| IC$_{50}$ (μg mL^{-1})	FSK	HEK293	HeLa	SKBR3	THP-1	A549
Sb-H	R	R	22.7	67.8	136.1	R
Sb-NP	R	R	11.7	34.8	R	R
Sb-NS	R	R	R	121.8	R	R
SbCl$_3$	285.6	160.4	7.6	10.9	95.5	R

Fig. 6 Cell viability histograms of the six tested cell lines treated with different concentrations of the three Sb-nanomaterials and SbCl3. Data represent the mean ± SD from three independent experiments performed in triplicate. Data analysis was performed using GraphPad Prism 8 software.

compare the cytotoxicity. Cell death was confirmed through the iodine propidium test (Fig. S9†).

In general, the Sb nanomaterials exhibited higher viability than the positive control SbCl$_3$, which presented the lowest IC$_{50}$ values. Interestingly, the three Sb-nanomaterials are biocompatible with the non-tumor cell lines, with only the positive control causing mild toxicity. Nevertheless, Sb nanomaterials present general toxicity against cancerous cell lines (Sb-NP > Sb-H > Sb-NS), but the cytotoxic effects cannot be generalized and are specific for each cell line and material, and they require a separate discussion.

In the case of THP-1, Sb-H is the only nanomaterial that exerts cytotoxicity, with an IC$_{50}$ of 136.1 μg mL^{-1}. For HeLa cells, both Sb-NP and Sb-H exhibit cytotoxicity, with the former showing the highest (IC$_{50}$ = 11.67 and 22.7 μg mL^{-1} respectively). Regarding SKBR3, all the nanomaterials showed cytotoxicity, highlighting Sb-NP as the most toxic (IC$_{50}$ = 34.8 μg mL^{-1}), followed by Sb-H (IC$_{50}$ = 67.8 μg mL^{-1}) and Sb-NS (IC$_{50}$ = 121.8 μg mL^{-1}). Surprisingly, A549 resulted in being resistant not only to every nanomaterial but also to the positive control at the tested concentration in contrast with previous reports, showing higher toxic effects for this cell line.[25] In light of these results, it is interesting to remark on the wide cytotoxic effects of Sb-H in tumoral cells, with only A549 presenting resistance, displaying larger potential biomedical applications than the other Sb-nanomaterials.

Interestingly, in terms of the different sizes and shapes of the Sb-nanomaterials, the small Sb-NP causes higher toxic effects on the tumor cell lines (HeLa, SKBR3). Its more rounded shape and small size ease its internalization,[46] and its evolution into toxic Sb oxidized species endows this Sb-nanomaterial with good chemotherapeutic effects. In turn, Sb-NS exhibits lower toxic effects not only due to its more difficult internalization (because of its larger size and elongated shape) but also due to its lower oxidation, which generates fewer toxic species in the cellular environment. Sb-H is expected to show the lowest cytotoxicity due to its large lateral size, hindering internalization. However, it exhibits intermediate toxicity among the tested Sb-nanomaterials, thereby exerting toxic effects in all the non-resistant tumor cell lines. We believe this behavior is due to the degradation suffered by the material in a biological environment, leading to the formation of smaller particles of easier internalization (similar in size and shape to the Sb-NP). Furthermore, its faster and complete oxidation quickly increases the intracellular levels of toxic Sb oxides, hindering the ability of tumor cells to escape cell death[43] and improving Sb-H chemotherapeutic potential. In this study, we focused on the acute cytotoxicity of the materials at 24 hours, and we cannot discard long-term toxicity or other effects, such as genotoxicity or epigenetic modifications, as the Sb-nanomaterials further degrade, which are beyond the scope of this work.

Considering these observations, it is now worth comparing the dark cytotoxicity of as-synthetized Sb-nanomaterials with previous reports where Sb-nanomaterials (nanosheets and nanoparticles) were protected by different chemical approaches. The PEG-coated nanoparticles showed good biocompatibility and were toxic only when irradiated with NIR light.[16] Similarly, PLGA-coated nanosheets and nanoparticles showed low toxicity before irradiation, with cytotoxic effects increased after light treatment.[21,22] Other types of coatings, such as cell membrane camouflage or CaCO$_3$ composites, have also been used, increasing the carrier biocompatibility.[17,26] As demonstrated for other nanomaterials, polymeric coatings increase the biocompatibility most likely by protecting the surface of the nanomaterials from the chemical reactive biological environment, improving their stability.[47] However, the final therapeutic effect of biomedical nanoplatforms relies directly on the nanomaterial-biological microenvironment interactions once released from its coating and remarks the importance of investigating as-synthesized-nanomaterial biological behavior to understand their effects.

In this regard, the more we explore the cytotoxicity exerted by Sb materials, the more we understand that it mostly depends on their initial chemical composition and their evolution under biological conditions. Indeed, XAS suggests that it is the oxidation of the materials that generates toxic species rather than the material. Thus, to assess the mechanism involved in the cytotoxic effect, it is crucial to investigate the biochemical pathway affected by treatment with naked Sb-nanomaterials.
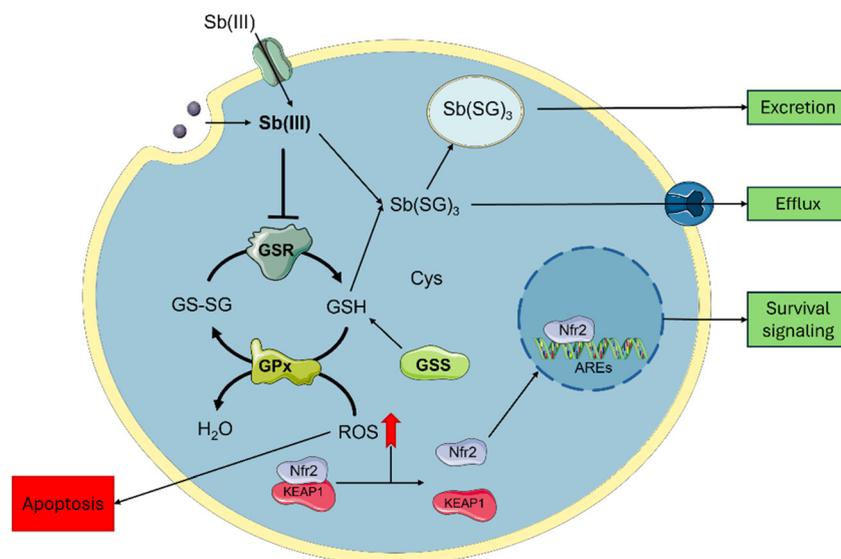
Cytotoxicity mechanisms

Sb-nanomaterial cytotoxic mechanisms have been scarcely studied; however, these are better known for Sb compounds and can be employed to rationalize one of their related nanomaterials (Scheme 2). Sb affects glutathione homeostasis in its trivalent state Sb(III) by binding to glutathione to form Sb-SG$_3$ complexes and promote its efflux.[18] Sb(III) can also inhibit the Glutathione Reductase (GSR) enzyme,[48] depleting the cellular glutathione pool and increasing cellular ROS. Furthermore, Sb(III) leads to yeast's DNA malfunction.[49] Similarly, Sb$_2$O$_3$ is known to induce cellular toxicity by increasing ROS generation.[43]

Regarding Sb nanomaterials, the cellular environment plays an important role in the oxidation and cytotoxicity of the materials. It has been demonstrated that under hypoxia conditions, Sb is oxidized to Sb(III), causing higher cytotoxic effects under normoxic conditions, where Sb can be oxidized to Sb(V) due to higher O$_2$ content.[22] This hypoxia-inducible cytotoxicity endorses few-layer antimonene with a great chemotherapeutic potential over other 2D materials by considering the advantage of the hypoxic tumoral environments to synergistically improve the treatment.

To correlate the cytotoxic mechanism of Sb-H with the production of oxidized Sb(III) (Scheme 2), we designed three complementary experiments aimed at understanding antimony intracellular levels, GSR enzyme-Sb interactions and ROS generation due to Sb-H incubation. The assays were performed on the HeLa cell as a sensible tumorous line, A549 as a tumorous resistant line and FSK as a non-tumorous line. Sb intracellular content was evaluated after incubation with Sb-H by recollect-

Scheme 2 Schematic representation of the cytotoxic mechanisms of Sb(III) in cells. In light green, enzymes related to the glutathione (GSH) metabolisms: glutathione reductase (GSR), glutathione synthetase (GSS) and glutathione peroxidase (GPx). The figure was partly generated using Servier Medical Art, provided by Servier, and licensed under a Creative Commons Attribution 3.0 unported license.
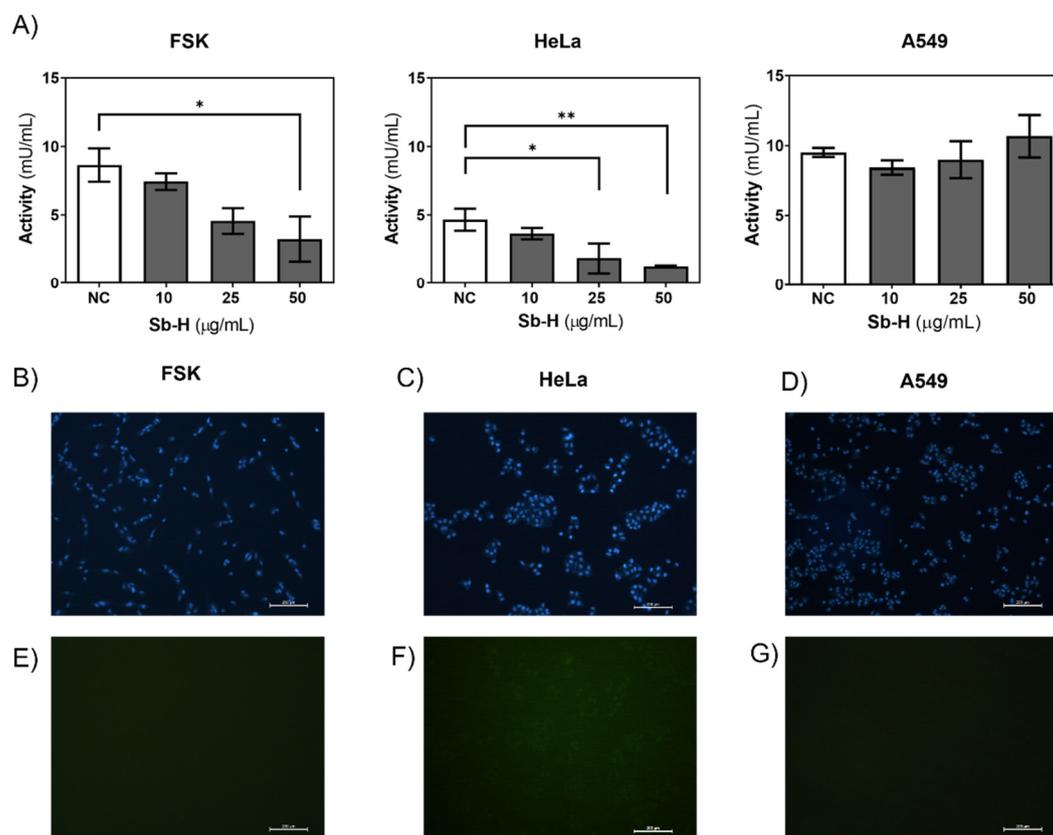

Fig. 7 (A) Activity of GSR enzyme after treating the cell lines with Sb-H at different concentrations and the Non-treated Cells (NC). Data are the mean SD of three independent experiments. Asterisks indicate significant differences relative to the control by the t-Student test (*$p < 0.05$, **$p < 0.01$). (B) and (E) FSK (C) and (F) HeLa (D) and (G) A549 fluorescence images showing Hoechst 33342 (top) used to visualize nuclei (DAPI filter) and Fluorescein (bottom) FITC filter to detect ROS formation in cells treated with Sb-H for 24 h using 6-carboxy-2′,7′-dichlodihydrorofluorescein diacetate probe (carboxy-H2DCF-DA). Images are representative of three independent experiments. Scale bars represent 200 microns.

ing the cellular extracts and analyzing them by ICP-MS (Fig. S10†). The analysis revealed a similar intracellular Sb content for the three lines in the range of 150–200 µg L^{-1} (corresponding to 3–4 ng per cell). This suggests comparable Sb-H internalization for all the investigated cell lines, indicating that the different cytotoxicities evaluated are probably not related to the different uptake ratios of the nanomaterial.

Furthermore, we investigated whether the activity of the GSR enzyme was affected by the Sb-H treatment. In the case of HeLa and FSK, GSR activity decreased upon Sb-H incubation (50 µg mL^{-1}) to 72.4% and 62.5%, respectively (Fig. 7A). In contrast, GSR activity in the A549 cell line exhibited an increase of 12.1%. It is important to note that the enzyme activity in the untreated FSK and A549 cells was 2-fold higher than that of the control HeLa cells; this may explain why even in front of a decreased activity for the FSK, no evident toxic effects were observed compared to HeLa cells.

Cellular ROS increase could be caused by a decrease in both GSR activity and/or ROS generation by the swift oxidation of Sb-H and can be one of the causes of cell death. For this purpose, cells were incubated with the Sb-H material and fluorescein derivate (H$_2$CDFDA), in which fluorescence is triggered by a reaction with intracellular ROS. The results obtained show that ROS production occurs only in HeLa cells, while little fluorescence was detected for both FSK and A549 cells (Fig. 7E, F, and G and Fig. S11†).

In light of these results, both the Sb-nanomaterials and the Sb(III) generated from their degradation can be internalized,[19,50] increasing the trivalent Sb inside the cells. This causes a decrease in the activity of the GSR in HeLa enough to reduce the pool of glutathione, causing ROS increase and viability decrease. The inhibition of GSR also occurs in non-tumoral cell lines, but no ROS production was observed, in agreement with the milder toxic effect observed in FSK. This difference can be associated with the different oxidative and metabolic activities of tumorous cells compared to non-tumors, causing Sb oxidation into its toxic specie Sb(III), leading to cell death.[22] Interestingly, the A549 cell line is also observed to be resistant to the positive control SbCl$_3$. This cell line is known to have higher levels of both the glutathione and the enzymes related to its production (GSR, GR),[51] and this could be the reason for their higher resistance. This may be related to the Nrf2 pathway, as depicted in Scheme 2, which is known to have a protective role against antimony toxicity,[43] and it is overexpressed in A549.[52]

Conclusions

In this work, we performed a thorough multidisciplinary study that combined material chemistry and biological investigation. Structural analysis, spectroscopic characterization, chemical stability, and cellular toxicity of three antimonene nanomaterials, Sb-H, Sb-NS, and Sb-NP were carried out. In situ synchrotron XAS analyses in biological conditions revealed the dynamic chemical oxidation process suffered by Sb-nano-

materials. Interestingly, while a similar initial oxidation state was observed for all Sb-nanomaterials, their evolution diverged to different degrees of oxidation upon incubation in cell culture media, highlighting the importance of the synthetic methodology on the stability of the materials. Regarding the dark cytotoxicity of the as-synthesized nanomaterials, cellular viability experiments have demonstrated that all the tested Sb-nanomaterials are non-harmful for healthy cells, with Sb-H the only nanomaterial inducing cytotoxicity in all non-resistant tumor cells. Thus, Sb-H's tumor-specific toxicity, together with its swift oxidation and degradation upon interaction with the biological environment, endows Sb-H with excellent chemotherapeutic properties.

Furthermore, we correlated the enhanced cytotoxic effects of Sb-H with its evolution into Sb-oxidized species. Enzymatic studies revealed Sb-H action in reducing GSR's activity in the non-resistant cell lines through the formation of Sb(III), leading to the dysregulation of the glutathione pool of the cell. Indeed, the production of ROS was detected for only the HeLa cell line, which exhibited cytotoxicity in the presence of Sb-H. These results shed light for the first time on the mechanisms causing the intrinsic cellular toxicity of Sb-nanomaterials, highlighting the effects caused by their chemical evolution on biological systems. Their controlled oxidation will open the doors to the development of on-demand synergic photoresponsive chemotherapy based on Sb-nanomaterials.

Experimental methodology

Materials

Antimony balls were purchased from Smart Elements (purity 99.98%) Technical grade octadecene (ODE, 90%), dodecanothiol (DDT, 99.9%), octadecanothiol (ODT, 98%), oleylamine (OA, 70%), antimony trichloride (SbCl3, 99.999%), and N-Methyl-2-Pyrrolidone (NMP) were purchased from Sigma Aldrich. Chloroform was obtained from Alfa Aesar. HPLC grade chloroform was obtained from Scharlab. Isopropyl alcohol (IPA, 99.8%) from Panreac. For cell culture experiments, Dulbecco's Modified Eagle Medium (DMEM), Roswell Park Memorial Institute (RPMI) 1640 medium, fetal bovine serum (FBS), and penicillin–streptomycin (1.0 × 10 5 U mL^{-1}, 1.0 × 105 µg mL^{-1}) were supplied by Invitrogen. Trypsin-EDTA (0.25%–0.02%) and glutamine (100 mM) solutions were provided by Cultek (Madrid, Spain).

Sb-H synthesis

The synthesis of both the antimony precursor and the resulting antimonene was carried out following the optimized methodology described by Torres et al.[27] The reactants (DDT, ODE and OA) were dried with molecular sieves overnight, degassed the liquids at 110 °C under vacuum overnight (12 h) and stored under argon before use. The dried and degassed solvents were used as feedstock for each injection.

For the SbCl3-DDT precursor, SbCl$_3$ (0.912 g, 4 mmol), DDT (4 mL), and ODE (6 mL) were added into a 50 mL 3-neck AMH.

The mixture was heated up under argon to 150 °C for 2 h. The signal that the reaction has occurred is a colour change from transparent to yellowish. Because the SbCl3-DDT precursor solution precipitates out of ODE at room temperature, it is pre-heated at 60 °C before its use.

OA (0.5 mL) and ODE (4.0 mL) were added into a 50 mL three-necked flask. Next, the flask was heated up to 300° C under argon; then, 1 mL of SbCl$_3$-DDT precursor solution was injected swiftly into the reaction system. After 10 s, the reaction was stopped and cooled down by immersing the flask into a water bath, and the final few-layer antimonene was obtained by centrifugation. To isolate the thickest nanosheets, the mixture was centrifuged twice at 13 400 rpm for 20 min and redispersed in CHCl$_3$.

Sb-NS synthesis

For the synthesis of Sb-NS, a standard liquid phase exfoliation (LPE) method is followed, previously reported in the literature by our group:[13] 10 mg of Sb powder are weighted and transferred into a 15 mL Falcon, and 10 mL of a dissolution 4 : 1 of 2-propanol : H$_2$O is added. The mixture is then sonicated in an ice bath with a fine microtip for 40 min using a 1 : 2 pulse and an amplitude of 40%. The resulting suspension is then centrifuged at 3000 rpm and 4 °C for 3 min. The supernatant is carefully recovered using a syringe and transferred to another 15 mL falcon, which is centrifuged at 10 000 rpm and 4 °C for 1 h. The supernatant is discarded carefully with a syringe, and the pellet is resuspended in 1 mL of 2-propanol and stored in a vial.

Sb-NP synthesis

Sb-NP was prepared following the protocol previously reported[21] with slight modifications: 300 mg of Sb powder is weighted and transferred into a 25 mL Falcon tube containing 16 mL of NMP. Next, the mixture is sonicated in an ice bath with a fine tip for 16 h, with a 1 : 2 pulse and an amplitude of 40%. Afterwards, a bath sonication in ice is performed for 24 h. Finally, the fine tip sonication is repeated for 16 h under the same conditions as in the first step. The falcon is then centrifuged at 12 000 rpm and 4 °C for 10 min (BeckmanJ-265XP, rotor JA25-50). Supernatant is recovered carefully with a syringe and is centrifugated at 20 000 rpm and 4 °C for 1 h. The supernatant is discarded carefully with a syringe, and the pellet is washed with EtOH. This step is repeated up to 3 times. After the last centrifugation, the supernatant is discarded carefully with a syringe, and the pellet is resuspended in a small volume of EtOH (800 μL^{-1} mL) and stored in a glass vial.

TEM/HRTEM

TEM images were obtained using a Hitachi 7800 TEM system with an accelerating voltage of 200 kV. The microscope has a multiscan charge-coupled device (CCD) camera ORIUS SC1000 and an OXFORD INCA X-Ray Energy Dispersive Spectroscopy (XEDS) microanalysis system. For the preparation of transmission electron microscopy (TEM) samples, the product obtained by centrifugation was dispersed in CHCl$_3$ and deposited on lacey formvar/carbon copper grids (300 mesh). HRTEM images were obtained using a FEI TECNAI G2 F20 S-TWIN HRTEM with an accelerating voltage of 200 kV, equipped with a CCD GATAN and an XEDS microanalysis system.

Scanning transmission electron microscopy (STEM)

High-resolution STEM, high-angle annular dark field and annular bright field images were obtained using a JEOLARM200cF microscope equipped with a spherical aberration corrector and a Gatan Quantum electron energy loss spectrometer at the Centro Nacional de Microscopía Electrónica (ICTS ELECMI) at UCM, Spain. Elemental composition maps were produced using multiple linear least squares fit of the data to reference EEL spectra. All data were acquired at an accelerating voltage of 80 kV. Measurements were performed for the M$_{4,5}$ absorption edge of the Sb to be able to obtain a good contrast on the signal. The M$_4$ and M$_5$ absorption edges result from transitions of 3d core electrons to unoccupied stares with p- and f-like symmetry, while the O K edge results from transitions of 1s electrons to available states with a 2p-like character.[53]

Raman spectroscopy

Raman spectroscopic characterization was carried out using a LabRAM HR Evolution confocal Raman microscope (Horiba). The measurements were conducted with an excitation wavelength of λ_{exc} = 633 nm. The laser was focused using a 100× objective (0.8 NA), thus leading to a laser spot with a diameter of $ca.$ 1 μm. A CCD camera was employed to collect the backscattered light that was dispersed by 1800 grooves per mm grating with a spectral resolution of ~1 cm^{-1}. The corresponding Raman spectra were then constructed by processing the data using Lab Spec 5 software.

XPS

XPS measurements were performed in an ultrahigh vacuum system ESCALAB210 (base pressure 1.0 × 10^{-10} mbar) from Thermo VG Scientific. Photoelectrons were excited using the Mg Kα line (1253.6 eV). Sputtering was performed with an Ar gun.

XRD

Surface X-ray powder diffraction patterns were obtained by employing a PANalytical Empyrean X-ray platform with a capillary platform and copper radiation (Cu Kα = 1.54178 Å). Measurements were carried out in triplicate in the 2-theta range 10–60° by employing a step size of 0.02° per step with an integration time of 1 s. Chloroform suspension of the samples was deposited on a glass slide at 37 °C to evaporate the solvent and form a homogeneous surface.

XAS

X-ray Absorption Spectroscopy (XAS) measurements were performed at the BL-22 (CLÆSS) beamline from the ALBA syn-

chrotron (Barcelona – Spain). Proposal: 2021095421. XANES and EXAFS Sb K-edge spectra were measured at room temperature in the transmission and fluorescence modes. XAS spectra were collected from 7590–8550 eV with a reduced step (0.2 eV) in the XANES region (7690–7750 eV), and the incident photon energy was calibrated using the first inflection point of the Sb K-edge from the Sb metallic reference.

Ex situ measurements were obtained from pellets composed of the nanomaterial together with cellulose and measured in fluorescence and transmission modes. The *in situ* measurements were carried out by measuring the nanomaterials incubated in DMEM supplemented with FBS. Once the nanomaterials were resuspended in the DMEM, a peristaltic pump was used to take the suspension through a capillary in which the synchrotron light was focused. During the recording, the cell culture media was kept at 37 °C.

Cell culture conditions

HeLa, FSK, A549, HEK293 and SKBR3 cells were grown in DMEM medium supplemented with 10% fetal bovine serum (FBS), 4 nM L-glutamine, 100 U mL^{-1} penicillin and 100 mg mL^{-1} streptomycin. The THP-I cell line was grown in RPlMI-1640 medium, supplemented with 10% FBS, 4 mM L-glutamine, 100 U mL^{-1} penicillin and 100 μg mL^{-1} streptomycin. All cell lines were cultured in exponential cell growth in 100 mm Petri dishes (P100) using a humidified incubator (37 °C, 5% CO$_2$ atmosphere), splitting twice a week when confluence reached 80–90%.

Cytotoxicity assay

The toxicity of Sb-nanomaterials in FSK, HeLa, HEK293, A549, THP-1 and SKBR3 cell lines was measured at different concentrations of the materials using an MTT assay. Cytotoxicity values were obtained from three independent experiments, $n = 3$. In each independent experiment, three technical replicates were used for each condition. First, cells were incubated in 96-well plates (HeLa and SKBR3 2500 cells per well, FSK 8000 cells per well, HEK293 cells per well, A549 cells per well, and THP-1 10 000 cells per well) with 100 μL per well of Gibco Dulbecco's Modified Eagle Medium (DMEM) at 37 °C in an atmosphere of 5% CO$_2$ for 24 h. Subsequently, the different materials were resuspended in DMEM medium, and the bath was sonicated for 5 min (amplitude 25%) to achieve a homogeneous suspension. Cells were treated with different concentrations of the antimonene-based materials ranging from 1.25 to 200 μg mL^{-1}, and incubated at 37 °C, 5% CO$_2$. For the incubation of the materials with the DMEM, nanomaterials were dried using a vacuum for 24 h to evaporate the organic solvent (chloroform), and the obtained pellet was resuspended in DMEM. After 24 h of treatment, 20 mL of MTT (2.5 mg mL^{-1}) was added to each well, and plates were incubated for 4 h under the same conditions. Finally, the medium was removed, and the purple product was solubilized in 100 mL of dimethyl sulfoxide (DMSO). The plates were read at 540 nm using a spectrophotometer. The experiment was performed at least three times, and the dose–response curves were determined

for each nanomaterial using the results of $n = 3$ with the GraphPad Prism 8 software, which was also used to obtain the corresponding IC50 values. Because of their electron-donor properties, Sb nanomaterials were reported as possible interfering agents with the compound employed for the cytotoxicity essay (3-(4,5-dimethylthiazol-2-yl)-2,5-diphenyltetrazolium bromide (MTT)), giving false positive results.[14,25] The interactions of the MTT were assessed for each nanomaterial, concluding that there was no interference for the tested concentrations. Moreover, a complementary cell viability test called Neutral Red Uptake (NRU) was used to observe the differences in the assay due to possible interference, with the difference between the tests being negligible.

Propidium iodine test

HeLa and FSK cells are cultured following the previous steps and treated with a concentration of 25 μg mL^{-1}. After 24 h, 50 μL of propidium iodine is added to each well, and the cells are observed under a fluorescent microscope. The red fluorescence (617 nm emission maxima) indicates the intercalation into the DNA, thus confirming the death of the cell (Fig. S9†).

GSR enzymatic activity assay

To analyze the activity of GSR after the treatment with Sb-H, cellular extracts of Sb-H-treated cells were prepared. Cells were seeded at a density of 50 000 cells per mL using 6-well plates and incubated for 24 h. Cells were subsequently treated for another 24 h with the indicated concentrations of Sb-H, followed by the recollection of the cells by scrapping and protein quantification of the cellular extracts, which were frozen at −20 °C. The activity of the GSR enzyme was then measured using the Glutathione Reductase Fluorescent Activity Kit (Invitrogen), following the instructions of the manufacturer. The values represent the mean of three independent experiments ($n = 3$).

Internalization of Sb

The amount of Sb internalized after the treatment with Sb-H was obtained by ICP-MS. Cells were seeded following the previous conditions, with a density of 50 000 cells per well. After 24 h, cells were treated with Sb-H at 25 μg mL^{-1}. After 24 h, cellular pellets after treatment were recollected and washed 3 times with PBS, followed by their membrane lysis to measure the Sb content. The measurement was performed by the SCSIE of the UV using ICPMS7900 (Agilent Technologies).

ROS production

To assess intracellular ROS production after treatment with Sb-H, cells were cultured as previously stated with a density of 25 000 cells per well in a 12-well plate. After 24 h, cells were treated with different concentrations of Sb-H, ranging from 10 to 50 μg mL^{-1}, together with 10 μg mL^{-1} SbCl$_3$ and 100 μM of *tert*-butyl hydroperoxide as positive control. 6-Carboxy-2′,7′-dichlodihydrorofluorescein diacetate probe (carboxy-H2DCF-DA) was added following the supplier instructions,

and after 24 h, the cells were imaged in an inverted fluorescent microscope (Leica).

Conflicts of interest

There are no conflicts to declare.

Acknowledgements

References

1 K. S. Novoselov, A. K. Geim, S. V. Morozov, D. Jiang, Y. Zhang, S. V. Dubonos, I. V. Grigorieva and A. A. Firsov, Electric Field Effect in Atomically Thin Carbon Films, *Science*, 2004, **306**, 666–669.

2 A. Jayakumar, A. Surendranath and M. Pv, 2D materials for next generation healthcare applications, *Int. J. Pharm.*, 2018, **551**, 309–321.

3 N. Rohaizad, C. C. Mayorga-Martinez, M. Fojtů, N. M. Latiff and M. Pumera, Two-dimensional materials in biomedical, biosensing and sensing applications, *Chem. Soc. Rev.*, 2021, **50**, 619–657.

4 M. A. Lucherelli, V. Oestreicher, M. Alcaraz and G. Abellán, Chemistry of two-dimensional pnictogens: emerging post-graphene materials for advanced applications, *Chem. Commun.*, 2023, **59**, 6453–6474.

5 N. R. Glavin, R. Rao, V. Varshney, E. Bianco, A. Apte, A. Roy, E. Ringe and P. M. Ajayan, Emerging Applications of Elemental 2D Materials, *Adv. Mater.*, 2020, **32**, 1904302.

6 K. Riehemann, S. W. Schneider, T. A. Luger, B. Godin, M. Ferrari and H. Fuchs, Nanomedicine—Challenge and Perspectives, *Angew. Chem., Int. Ed.*, 2009, **48**, 872–897.

7 T. Sun, Y. S. Zhang, B. Pang, D. C. Hyun, M. Yang and Y. Xia, Engineered Nanoparticles for Drug Delivery in Cancer Therapy, *Angew. Chem., Int. Ed.*, 2014, **53**, 12320–12364.

8 M. Qiu, W. Xiu Ren, T. Jeong, M. Won, G. Young Park, D. Kipkemoi Sang, L.-P. Liu, H. Zhang and J. Seung Kim, Omnipotent phosphorene: a next-generation, two-dimensional nanoplatform for multidisciplinary biomedical applications, *Chem. Soc. Rev.*, 2018, **47**, 5588–5601.

9 M. Tatullo, F. Genovese, E. Aiello, M. Amantea, I. Makeeva, B. Zavan, S. Rengo and L. Fortunato, Phosphorene Is the New Graphene in Biomedical Applications, *Materials*, 2019, **12**, 2301.

10 X. Liu, B. Gaihre, M. N. George, Y. Li, M. Tilton, M. J. Yaszemski and L. Lu, 2D phosphorene nanosheets, quantum dots, nanoribbons: synthesis and biomedical applications, *Biomater. Sci.*, 2021, **9**, 2768–2803.

11 J. A. Carrasco, P. Congost-Escoin, M. Assebban and G. Abellán, Antimonene: a tuneable post-graphene material for advanced applications in optoelectronics, catalysis, energy and biomedicine, *Chem. Soc. Rev.*, 2023, **52**, 1288–1330.

12 P. Ares, F. Aguilar-Galindo, D. Rodríguez-San-Miguel, D. A. Aldave, S. Díaz-Tendero, M. Alcamí, F. Martín, J. Gómez-Herrero and F. Zamora, Mechanical Isolation of Highly Stable Antimonene under Ambient Conditions, *Adv. Mater.*, 2016, **28**, 6332–6336.

13 C. Gibaja, D. Rodriguez-San-Miguel, P. Ares, J. Gómez-Herrero, M. Varela, R. Gillen, J. Maultzsch, F. Hauke, A. Hirsch, G. Abellán and F. Zamora, Few-Layer Antimonene by Liquid-Phase Exfoliation, *Angew. Chem., Int. Ed.*, 2016, **55**, 14345–14349.

14 G. Abellán, P. Ares, S. Wild, E. Nuin, C. Neiss, D. R.-S. Miguel, P. Segovia, C. Gibaja, E. G. Michel, A. Görling, F. Hauke, J. Gómez-Herrero, A. Hirsch and F. Zamora, Noncovalent Functionalization and Charge Transfer in Antimonene, *Angew. Chem., Int. Ed.*, 2017, **56**, 14389–14394.

15 M. M. Ayyub, M. Barua, S. Acharya and C. N. R. Rao, Covalent Functionalization of Antimonene and Bismuthene Nanosheets, *Small*, 2022, **18**, 2203554.

16 W. Tao, X. Ji, X. Xu, M. A. Islam, Z. Li, S. Chen, P. E. Saw, H. Zhang, Z. Bharwani, Z. Guo, J. Shi and O. C. Farokhzad, Antimonene Quantum Dots: Synthesis and Application as Near-Infrared Photothermal Agents for Effective Cancer Therapy, *Angew. Chem.*, 2017, **129**, 12058–12062.

17 J. Wu, X. Cai, G. R. Williams, Z. Meng, W. Zou, L. Yao, B. Hu, Y. Chen and Y. Zheng, 2D antimonene-integrated composite nanomedicine for augmented low-temperature photonic tumor hyperthermia by reversing cell thermoresistance, *Bioact. Mater.*, 2022, **10**, 295–305.

18 S. Wyllie and A. H. Fairlamb, Differential toxicity of antimonial compounds and their effects on glutathione homeostasis in a human leukaemia monocyte cell line, *Biochem. Pharmacol.*, 2006, 11.

19 W. Tao, X. Ji, X. Zhu, L. Li, J. Wang, Y. Zhang, P. E. Saw, W. Li, N. Kong, M. A. Islam, T. Gan, X. Zeng, H. Zhang,

M. Mahmoudi, G. J. Tearney and O. C. Farokhzad, Two-Dimensional Antimonene-Based Photonic Nanomedicine for Cancer Theranostics, *Adv. Mater.*, 2018, **30**, e1802061.

20 C. J. Boreiko and T. G. Rossman, Antimony and its compounds: Health impacts related to pulmonary toxicity, cancer, and genotoxicity, *Toxicol. Appl. Pharmacol.*, 2020, **403**, 115156.

21 Y. Duo, Y. Huang, W. Liang, R. Yuan, Y. Li, T. Chen and H. Zhang, Ultraeffective Cancer Therapy with an Antimonene–Based X–Ray Radiosensitizer, *Adv. Funct. Mater.*, 2020, **30**, 1906010.

22 M. Qiu, Y. Duo, W. Liang, Y. Yang, B. Zhang, Z. Xie, X. Yang, G. Wang, N. Xie, G. Nie, O. A. Alhartomy, A. A. Alghamdi, S. Wageh, Y. Cao and H. Zhang, Nanopoxia: Targeting Cancer Hypoxia by Antimonene-Based Nanoplatform for Precision Cancer Therapy, *Adv. Funct. Mater.*, 2021, **31**, 2104607.

23 X. Niu, Y. Li, Y. Zhang, Z. Zhou and J. Wang, Greatly Enhanced Photoabsorption and Photothermal Conversion of Antimonene Quantum Dots through Spontaneously Partial Oxidation, *ACS Appl. Mater. Interfaces*, 2019, **11**, 17987–17993.

24 M. Assebban, C. Gibaja, M. Fickert, I. Torres, E. Weinreich, S. Wolff, R. Gillen, J. Maultzsch, M. Varela, S. Tan Jun Rong, K. P. Loh, E. G. Michel, F. Zamora and G. Abellán, Unveiling the oxidation behavior of liquid-phase exfoliated antimony nanosheets, *2D Mater.*, 2020, **7**, 025039.

25 H. L. Chia, N. M. Latiff, R. Gusmão, Z. Sofer and M. Pumera, Cytotoxicity of Shear Exfoliated Pnictogen (As, Sb, Bi) Nanosheets, *Chem. – Eur. J.*, 2019, **25**, 2242–2249.

26 G. Lu, C. Lv, W. Bao, F. Li, F. Zhang, L. Zhang, S. Wang, X. Gao, D. Zhao, W. Wei and H. Xie, Antimonene with two-orders-of-magnitude improved stability for high-performance cancer theranostics, *Chem. Sci.*, 2019, **10**, 4847–4853.

27 I. Torres, M. Alcaraz, R. Sanchis-Gual, J. A. Carrasco, M. Fickert, M. Assebban, C. Gibaja, C. Dolle, D. A. Aldave, C. Gómez-Navarro, E. Salagre, E. G. Michel, M. Varela, J. Gómez-Herrero, G. Abellán and F. Zamora, Continuous-Flow Synthesis of High-Quality Few-Layer Antimonene Hexagons, *Adv. Funct. Mater.*, 2021, 2101616.

28 C. Gibaja, M. Assebban, I. Torres, M. Fickert, R. Sanchis-Gual, I. Brotons, W. S. Paz, J. J. Palacios, E. G. Michel, G. Abellán and F. Zamora, Liquid phase exfoliation of antimonene: systematic optimization, characterization and electrocatalytic properties, *J. Mater. Chem. A*, 2019, **7**, 22475–22486.

29 L. Peng, S. Ye, J. Song and J. Qu, Solution-Phase Synthesis of Few-Layer Hexagonal Antimonene Nanosheets via Anisotropic Growth, *Angew. Chem., Int. Ed.*, 2019, **58**, 9891–9896.

30 J. Zhang, S. Ye, Y. Sun, F. Zhou, J. Song and J. Qu, Soft-template assisted synthesis of hexagonal antimonene and bismuthene in colloidal solutions, *Nanoscale*, 2020, **12**, 20945–20951.

31 M. Lotya, A. Rakovich, J. F. Donegan and J. N. Coleman, Measuring the lateral size of liquid-exfoliated nanosheets

with dynamic light scattering, *Nanotechnology*, 2013, **24**, 265703.

32 S. Wolff, R. Gillen, M. Assebban, G. Abellán and J. Maultzsch, Two-Dimensional Antimony Oxide, *Phys. Rev. Lett.*, 2020, **124**, 126101.

33 P. Ares, J. J. Palacios, G. Abellán, J. Gómez-Herrero and F. Zamora, Recent Progress on Antimonene: A New Bidimensional Material, *Adv. Mater.*, 2018, **30**, 1703771.

34 *Lange's Handbook of Chemistry*, ed. J. G. Speight, McGraw-Hill Education, 17th edn, 2017.

35 T. W. Capehart, J. F. Herbst, R. K. Mishra and F. E. Pinkerton, X-ray-absorption edge shifts in rare-earth–transition-metal compounds, *Phys. Rev. B: Condens. Matter Mater. Phys.*, 1995, **52**, 7907–7914.

36 G. Abellán, S. Wild, V. Lloret, N. Scheuschner, R. Gillen, U. Mundloch, J. Maultzsch, M. Varela, F. Hauke and A. Hirsch, Fundamental Insights into the Degradation and Stabilization of Thin Layer Black Phosphorus, *J. Am. Chem. Soc.*, 2017, **139**, 10432–10440.

37 T. Gupta, K. Elibol, S. Hummel, M. Stöger-Pollach, C. Mangler, G. Habler, J. C. Meyer, D. Eder and B. C. Bayer, Resolving few-layer antimonene/graphene heterostructures, *npj 2D Mater. Appl.*, 2021, **5**, 1–11.

38 C. Martín, K. Kostarelos, M. Prato and A. Bianco, Biocompatibility and biodegradability of 2D materials: graphene and beyond, *Chem. Commun.*, 2019, **55**, 5540–5546.

39 M. A. Lucherelli, X. Qian, P. Weston, M. Eredia, W. Zhu, P. Samorì, H. Gao, A. Bianco and A. von dem Bussche, Boron Nitride Nanosheets Can Induce Water Channels Across Lipid Bilayers Leading to Lysosomal Permeabilization, *Adv. Mater.*, 2021, 2103137.

40 D. A. Jasim, L. Newman, A. F. Rodrigues, I. A. Vacchi, M. A. Lucherelli, N. Lozano, C. Ménard-Moyon, A. Bianco and K. Kostarelos, The impact of graphene oxide sheet lateral dimensions on their pharmacokinetic and tissue distribution profiles in mice, *J. Controlled Release*, 2021, **338**, 330–340.

41 H. Lin, D.-K. Ji, M. A. Lucherelli, G. Reina, S. Ippolito, P. Samorì and A. Bianco, Comparative Effects of Graphene and Molybdenum Disulfide on Human Macrophage Toxicity, *Small*, 2020, **16**, 2002194.

42 T. Loret, L. A. V. de Luna, M. A. Lucherelli, A. Fordham, N. Lozano, A. Bianco, K. Kostarelos and C. Bussy, Lung Persistence, Biodegradation, and Elimination of Graphene-Based Materials are Predominantly Size-Dependent and Mediated by Alveolar Phagocytes, *Small*, 2023, **19**, 2301201.

43 X. Jiang, Z. An, C. Lu, Y. Chen, E. Du, S. Qi, K. Yang, Z. Zhang and Y. Xu, The protective role of Nrf2-Gadd45b against antimony-induced oxidative stress and apoptosis in HEK293 cells, *Toxicol. Lett.*, 2016, **256**, 11–18.

44 T. Titma, R. Shimmo, J. Siigur and A. Kahru, Toxicity of antimony, copper, cobalt, manganese, titanium and zinc oxide nanoparticles for the alveolar and intestinal epithelial barrier cells in vitro, *Cytotechnology*, 2016, **68**, 2363–2377.

45 R. Greco, G. García-Lainez, J. Oliver-Meseguer, C. Marini, I. Domínguez, M. López-Haro, J. C. Hernández-Garrido, J. P. Cerón-Carrasco, I. Andreu and A. Leyva-Pérez, Cytotoxic sub-nanometer aqueous platinum clusters as potential anti-tumoral agents, *Nanoscale Adv.*, 2022, **4**, 5281–5289.

46 H. Hadji and K. Bouchemal, Effect of micro- and nano-particle shape on biological processes, *J. Controlled Release*, 2022, **342**, 93–110.

47 J. S. Suk, Q. Xu, N. Kim, J. Hanes and L. M. Ensign, PEGylation as a strategy for improving nanoparticle-based drug and gene delivery, *Adv. Drug Delivery Rev.*, 2016, **99**, 28–51.

48 M. L. Cunningham, M. J. Zvelebil and A. H. Fairlamb, Mechanism of inhibition of trypanothione reductase and glutathione reductase by trivalent organic arsenicals, *Eur. J. Biochem.*, 1994, **221**, 285–295.

49 I. Litwin, S. Mucha, E. Pilarczyk, R. Wysocki and E. Maciaszczyk-Dziubinska, Complex Mechanisms of Antimony Genotoxicity in Budding Yeast Involves Replication and Topoisomerase I-Associated DNA Lesions, Telomere Dysfunction and Inhibition of DNA Repair, *Int. J. Mol. Sci.*, 2021, **22**(9), 4510.

50 E. Maciaszczyk-Dziubinska, D. Wawrzycka and R. Wysocki, Arsenic and Antimony Transporters in Eukaryotes, *Int. J. Mol. Sci.*, 2012, **13**, 3527–3548.

51 E. L. Hatcher, Y. Chen and Y. J. Kang, Cadmium resistance in A549 cells correlates with elevated glutathione content but not antioxidant enzymatic activities, *Free Radicals Biol. Med.*, 1995, **19**, 805–812.

52 M.-H. Kweon, V. M. Adhami, J.-S. Lee and H. Mukhtar, Constitutive overexpression of Nrf2-dependent heme oxyge-nase-1 in A549 cells contributes to resistance to apoptosis induced by epigallocatechin 3-gallate, *J. Biol. Chem.*, 2006, **281**, 33761–33772.

53 R. F. Egerton, *Electron Energy-Loss Spectroscopy in the Electron Microscope*, Springer US, Boston, MA, 1996.